Research Article

Inactive Al^{3+}-doped La(CoCrFeMnNiAl$_x$)$_{1/(5+x)}$O$_3$ high-entropy perovskite oxides as high performance supercapacitor electrodes

Meng GUO, Yufeng LIU, Fengnian ZHANG, Fuhao CHENG,
Chufei CHENG, Yang MIAO[*], Feng GAO, Jun YU

College of Materials Science and Engineering, Taiyuan University of Technology, Taiyuan 030024, China

© The Author(s) 2022.

Abstract: A series of high-entropy perovskite oxides (HEPOs) La(CoCrFeMnNiAl$_x$)$_{1/(5+x)}$O$_{3-\delta}$ ($x = 0.4$, 0.5, 0.6, and 0.7) have been synthesized by coprecipitation method combined with calcination process and explored as electrodes for supercapacitors. The crystal structure, microstructure, and elemental composition of HEPOs were investigated by X-ray diffraction (XRD), scanning electron microscopy (SEM), transmission electron microscopy (TEM), and energy-dispersive X-ray spectroscopy (EDS) in detail. The electrochemical properties of HEPOs as supercapacitor electrodes were elucidated. The specific capacitances of HEPOs ($x = 0.4$, 0.5, 0.6, and 0.7) are 281.84, 353.65, 325.60, and 259.30 F/g at the current density of 1 A/g, respectively. After 2000 cycles, the specific capacitances of HEPOs ($x = 0.4$, 0.5, 0.6, and 0.7) remain 85.01%, 88.61%, 86.37%, and 91.25%, respectively. Such outstanding electrochemical properties can be attributed to the entropy-stabilized structure caused by mixed six cations in B-site and the Al^{3+}-doping suppressing active ion aggregation during charge–discharge process. This research highlights the potential of HEPOs as electrodes for supercapacitors.

Keywords: high-entropy oxides (HEOxs); perovskite structure; Al^{3+}-doping; supercapacitors

1 Introduction

In recent years, the ever-growing energy crisis leads to an increasing demand for the renewable energies such as solar energy, geothermal energy, and tidal energy [1–3]. Thus, it is urgent to develop a sustainable and renewable energy storage equipment to effectively store and utilize these energy resources. Among all the energy storage devices, supercapacitors have the potential to be the most promising electrochemical cells in the coming future owing to the superior advantages such as high power density, favorable cyclic performance, rapid charge rates, and safe operation [4–6].

According to the charge storage mechanisms, supercapacitor can be generally divided into electrical double layer capacitor relying on the adsorption and desorption of ions at the interface of electrode–electrolyte, and pseudocapacitor depending on the reversible faradaic redox reaction over the surface of the active materials [7,8]. Conventional carbonaceous materials used as electrodes for the former exhibit long cycle life and high power density [9,10]. Pseudocapacitive materials including conductive polymers and transition metal oxides/hydroxides have high specific capacitance and energy density [11–13]. However, the low capacity of carbonaceous materials and the volume change during

---

* Corresponding author.
E-mail: miaoyang198781@163.com

charge–discharge process of pseudocapacitive materials limit the further practical development. Transition metal oxide-based perovskite materials can overcome the volume expansion by using perovskite-based oxygen intercalation mechanisms [14,15]. Meanwhile, perovskite oxides can achieve high theoretical capacity and cycle stability due to stable structure and rich oxygen vacancy. So, it is essential for the development of new energy storage devices to explore new perovskite materials.

Rost *et al.* [16] first extended the field of high-entropy materials to oxide system, and successfully synthesized $(Mg_{0.2}Ni_{0.2}Co_{0.2}Cu_{0.2}Zn_{0.2})O$ high-entropy oxide (HEOx) with rock salt structure, in which configurational entropy is the key to stabilize rock salt structure. In subsequent investigation, HEOxs with different crystal structures and properties are gradually explored [17]. As of today, the reported HEOx types comprise high-entropy perovskites [18], high-entropy spinels [19], high-entropy fluorite oxides [20], high-entropy pyrochlores [21], high-entropy lanthanide sesquioxides [22], and bixbyite structured HEOxs [23]. Moreover, these new oxides show interesting and peculiar properties compared with binary or doped oxide systems, such as catalytic performance [24], energy storage [25], colossal dielectric constant [26], and low thermal conductivity [27].

Up to date, HEOxs, as electrode materials of energy storage devices, have attracted increasing attention due to their excellent electrochemical performance [28,29]. Bérardan *et al.* [30] first reported Li^+ conductivity of rock-salt structure HEOx at room temperature (10^{-3} S/cm). Subsequently, Qiu *et al.* [31] explored that $(Co_{0.2}Cu_{0.2}Mg_{0.2}Ni_{0.2}Zn_{0.2})O$ HEOx as an anode material for lithium ion batteries (LIBs) exhibits superior cycling stability owing to the stabilization effect of configurational entropy. And they also demonstrated that inactive MgO in $(Co_{0.2}Cu_{0.2}Mg_{0.2}Ni_{0.2}Zn_{0.2})O$ anode could prevent the agglomeration of active metal oxides, resulting in higher cycle stability [31], which provides a new idea for the design of HEOxs. Recently, high-entropy perovskite oxides (HEPOs) have also been applied to the LIBs, and $((BiNa)_{1/5}(LaLi)_{1/5}(CeK)_{1/5}Ca_{1/5}Sr_{1/5})TiO_3$ as anode material provides outstanding cycle capacity [32]. However, HEPOs have not been extensively researched for supercapacitors.

Based on the above thoughts, we try to dope with inactive ions at the B-site to improve the electrochemical properties of HEPOs. Al^{3+} is selected as the doped ion, because it is an inactive ion that can prevent the agglomeration of active metal oxides, and its ion radius

is quite different from other B-site ions that can produce lattice distortion and defects to retard crack propagation. A series of $La(CoCrFeMnNiAl_x)_{1/(5+x)}O_{3-\delta}$ ($x = 0.4, 0.5, 0.6$, and 0.7) have been synthesized by coprecipitation method combined with calcination process. The crystal structure and morphology of HEPOs were analyzed by X-ray diffraction (XRD), scanning electron microscopy (SEM), and transmission electron microscopy (TEM). The electrochemical properties of HEPOs as supercapacitor electrodes were investigated.

2 Experimental procedure

2.1 Synthesis of HEPOs

The base powders of $La(CoCrFeMnNiAl_x)_{1/(5+x)}O_{3-\delta}$ ($x = 0, 0.3, 0.4, 0.5, 0.6, 0.7$, and 0.8) were prepared by coprecipitation method combined with calcination process. $La(NO_3)_3 \cdot 6H_2O$, $Co(NO_3)_2 \cdot 6H_2O$, $Cr(NO_3)_3 \cdot 9H_2O$, $Fe(NO_3)_3 \cdot 9H_2O$, $Mn(NO_3)_2 \cdot 4H_2O$, $Ni(NO_3)_2 \cdot 6H_2O$, and $Al(NO_3)_3 \cdot 9H_2O$ (99.9%, Aladdin Biochemical Technology Co., Ltd.) were used for preparing the aqueous solutions. Na_2CO_3 (99.9%, Bangrui New Material Technology Co., Ltd.) was used as the precipitating agent. Initially, proper amount of nitrates were dissolved in deionized water to obtain solution (A). Na_2CO_3 was dissolved in deionized water to form solution (B). The solution (B) was slowly added into solution (A) with continuously stirring. When the pH value of the mixed solution was controlled to be 10 and kept unchanged for 30 min, the adding can be stopped. After 10 h at room temperature, the co-precipitate was filtered, repeatedly washed with deionized water, and dried overnight at 60 ℃. The co-precipitate was calcined at 1200 ℃ for 2 h to obtain perovskite oxides.

2.2 Sample characterization

XRD data were performed using the Ultima IV diffractometer (Rigaku), with Cu Kα radiation ($\lambda = 1.5406 \times 10^{-10}$ m), within 10°–90° range. The thermal behavior of powders was analyzed by thermogravimetry, differential thermal gravity, and the differential scanning calorimeter (TG/DTG/DSC, Mettler-Toledo) in air atmosphere (50 mL/min), with 10 ℃/min heating rate from room temperature to 1300 ℃. The phase structures and lattice parameters of powders were determined by performing Rietveld refinement with $La(Co_{0.5}Fe_{0.5})O_3$ as crystallographic information file (CIF) structure files and GSAS software. The morphology and composition

of the samples were detected by the scanning electron microscope (Lyra3, Tescan) equipped with an energy-dispersive X-ray spectroscope (Oxford Instruments) detector. The crystal structure and microstructure of powders were investigated by the transmission electron microscope (Tecnai G2 F30, FEI). Raman spectra were recorded using a Raman microscope (DXR2xi, Thermo Scientific), with 633 nm InGaN laser in the range of 250–2000 cm^{-1}. The acquisition time of each measurement was 10 s with two exposures.

2. 3   Electrochemical measurements

The HEPO powders (80 wt%), acetylene carbon black (10 wt%), and polyvinylidene fluoride (PVDF) binder (10 wt%) in N-methyl-2-pyrrolidone (NMP) were mixed to form a slurry. The slurry was evenly coated on the foam nickel (1 cm × 1 cm), and then dried for 12 h at 60 ℃. Finally, the dried foam nickel was made into working electrode under the pressure of 10 MPa for more than 10 s. The electrochemical properties of HEPOs for supercapacitor electrodes were measured in standard three electrode system in 2 mol/L KOH solution, with a platinum foil as the counter electrode and a saturated calomel electrode as the reference electrode. The cyclic voltammetry (CV) and galvanostatic charge–discharge (GCD) tests were implemented on an electrochemical workstation (CHI660D, Shanghai Chenhua Co., Ltd.) with potential window of 0–0.5 V at different scan rates and current densities. The electrochemical impedance spectroscopy (EIS) measurements were performed in the frequency region from 10 mHz to 100 kHz with an alternating current (AC) signal amplitude of 5 mV.

3   Results and discussion

3. 1   Structure characterization of HEPO materials

The XRD patterns of the synthesized powders are shown in Fig. 1. It can be seen that with the increase of Al^{3+} content, the phase structure changes from orthorhombic *Pnma* to *R*-3*c* structure, which can be explained by an increase of the Goldschmidt tolerance factor (*t*) becoming closer to 1 [33], due to the decrease of the average ionic radius of B-site. When HEPOs with *x* range from 0.4, 0.5, 0.6, to 0.7, no impurities can be observed in the samples. The HEPOs show a single-phase perovskite structure with *R*-3*c* (167) space group.
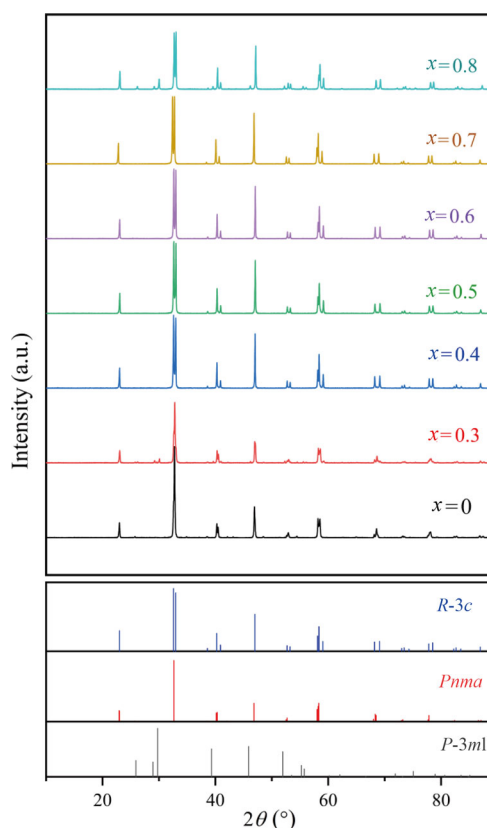
Fig. 1   XRD patterns of La(CoCrFeMnNiAl$_x$)$_{1/(5+x)}$O$_{3-\delta}$.

However, additional reflections are visible in the case of La(CoCrFeMnNiAl$_{0.3}$)$_{1/5.3}$O$_{3-\delta}$, which could not be unambiguously identified. The secondary phase is more clearly visible for *x* = 0.8 sample, indexed as *P*-3*m*1, which was identified as La$_2$O$_3$. Excessive Al^{3+}-doping leads to a bigger increase of *t* because of the smaller ionic radius of Al^{3+} than that of host transition-metal ions. Only *t* in a certain range can ensure the formation of the single-phase structure.

The TG–DSC pattern of La(CoCrFeMnNiAl$_{0.5}$)$_{1/5.5}$O$_3$ powder is shown in Fig. 2. According to the DTG and DSC curves, it can be seen that mass loss stage appears at about 761 ℃, which should correspond to the decomposition of carbonate. At about 889 ℃, small exothermal peaks and mass loss appear on the curve, which may correspond to the decompose of La$_2$O$_2$CO$_3$. The weight loss peak at 1153 ℃ with a sharp exothermal peak may be accompanied by the phase transition of HEPOs.

The Rietveld-refined XRD patterns of HEPOs are shown in Fig. 3. The basic structural data obtained by the Rietveld refinements of the XRD patterns are presented in Table 1. The HEPOs were normalized to provide the quasi-cubic parameters (volume and lattice
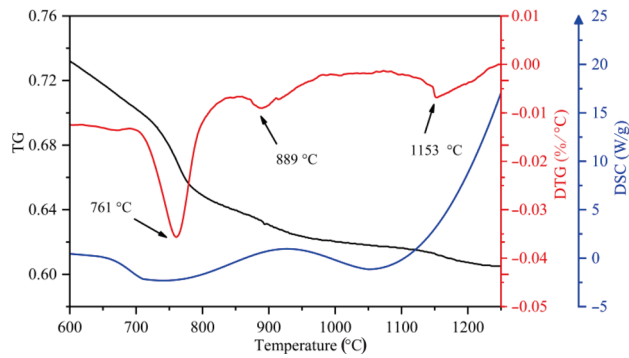
Fig. 2 TG–DSC patterns of La(CoCrFeMnNiAl$_{0.5}$)$_{1/5.5}$O$_{3-\delta}$.

constant a_0) calculated under the assumption that the rhombohedral unit cell is 6 times larger compared to the equivalent cubic. As can be seen, the lattice constant a_0 decreases with the increase of Al^{3+} content because of the smaller ionic radius (0.535×10^{-10} m) of Al^{3+} than those of host transition-metal ions [34]. Importantly, the decrease of a_0 indicates that the charge compensation mechanism in HEPOs is mainly through the oxidation of B-site cations rather than the formation of a significant amount of the oxygen vacancies. If the oxygen vacancies play a leading role, an
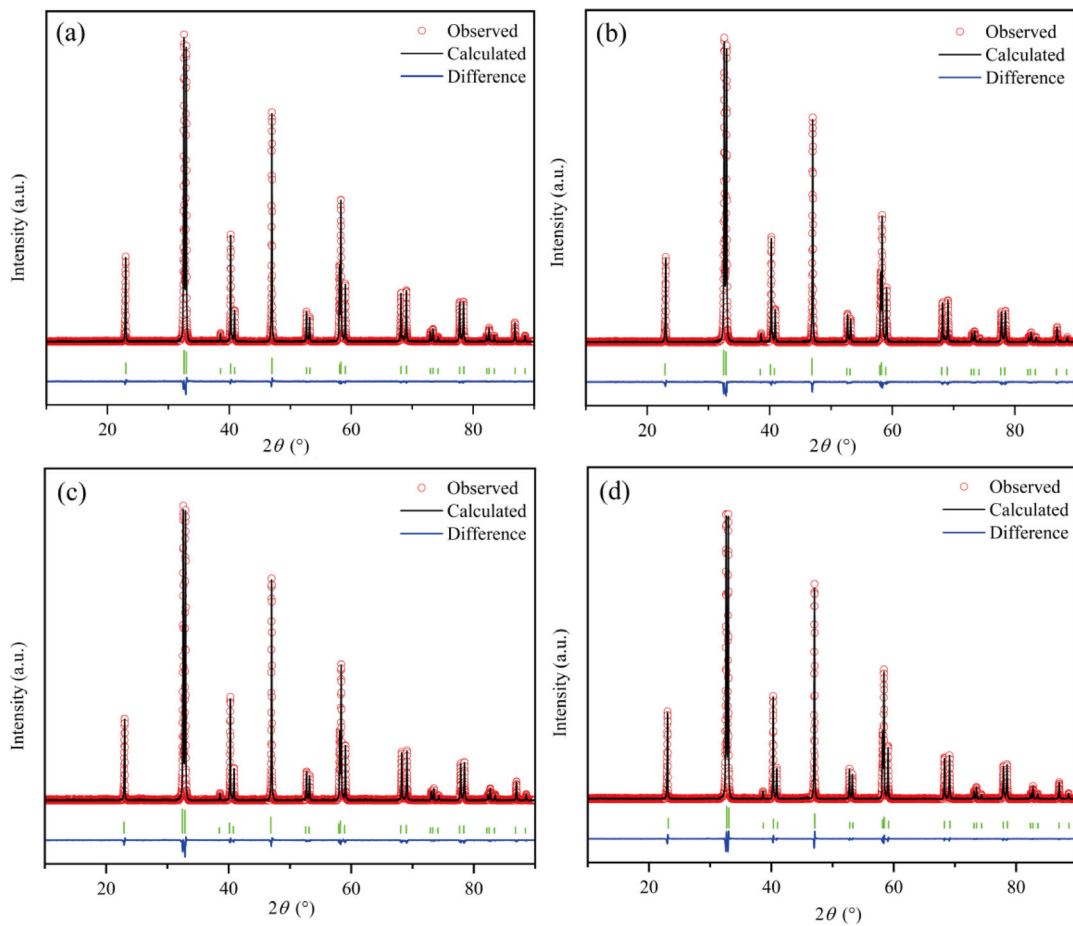

Fig. 3 Rietveld-refined XRD patterns of La(CoCrFeMnNiAl$_x$)$_{1/(5+x)}$O$_{3-\delta}$: (a) $x = 0.4$, (b) $x = 0.5$, (c) $x = 0.6$, and (d) $x = 0.7$.

Table 1 Calculated lattice constants of the obtained La(CoCrFeMnNiAl$_x$)$_{1/(5+x)}$O$_{3-\delta}$ perovskite materials

Composition	a (10^{-10} m)	b (10^{-10} m)	c (10^{-10} m)	Normalized cell volume (Å^3)	a_0 (Å)
La(CoCrFeMnNiAl$_{0.4}$)$_{1/5.4}$O$_{3-\delta}$	5.4994(1)	5.4994(1)	13.2366(4)	57.7818(3)	3.8660(1)
La(CoCrFeMnNiAl$_{0.5}$)$_{1/5.5}$O$_{3-\delta}$	5.4969(1)	5.4969(1)	13.2369(2)	57.7293(2)	3.8648(1)
La(CoCrFeMnNiAl$_{0.6}$)$_{1/5.6}$O$_{3-\delta}$	5.4937(3)	5.4937(3)	13.2358(1)	57.6588(1)	3.8632(1)
La(CoCrFeMnNiAl$_{0.7}$)$_{1/5.7}$O$_{3-\delta}$	5.4912(2)	5.4912(2)	13.2337(1)	57.5974(2)	3.8619(1)

Note: a_0 is the normalized quasi-cubic cell parameter.

increase of the unit cell volume can occur, caused by the chemical expansion [35] rather than a decrease. Moreover, the lattice contraction can enhance the binding force among the main atoms in the perovskite internal structure and produce a more stable crystal structure during the charge–discharge cycle [36]. Meanwhile, the Al^{3+}-doping increases the configurational entropy to further improve the crystal structural stability.

The morphology of $La(CoCrFeMnNiAl_{0.5})_{1/5.5}O_3$ was examined precisely by high-resolution transmission electron microscopy (HRTEM) analysis. The lattice spacings of 0.274, 0.386, and 0.239 nm, corresponding to the (110), (012), and (202) planes of the HEPO structure, respectively, can be seen in Figs. 4(a) and 4(b). The SEM micrographs of $La(CoCrFeMnNiAl_{0.5})_{1/5.5}O_{3-\delta}$ and $La(CoCrFeMnNiAl_{0.7})_{1/5.7}O_{3-\delta}$ are presented in Figs. 4(c) and 4(d). The primary grain sizes in the SEM micrographs of HEPOs are roughly about 0.2–0.5 μm. The small grain size proves that the grain growth is restrained by the extremely disordered grain interior caused by mixed six cations in B-site [37].

Figures 4(e) and 4(f) show the EDS mappings of the two samples to verify elements distribution. For the EDS mappings of HEPOs, it can be seen that some elements are uniformly distributed. Partial unevenly distributed elements do not affect the formation of the single-phase structure of HEOxs.

Raman spectroscopy is an effective method to further elucidate the nature of bonding in materials. The Raman spectra of HEPO materials are recorded in Fig. 5. Two main bands can be clearly seen near ca. 540 and 650 cm^{-1}, as well as a few low-intensity bands, representing similar characteristics for previous perovskite materials [38]. The obtained positions and intensities of the two main bands are summarized detailedly in Table 2. The low-intensity bands are attributed to the vibration of the lanthanum sublattice, mainly due to the relative motion of these cations with respect to the BO_6 octahedra [39]. The two main bands can be deconvoluted into at least three independent components, and their existence is related to the bending (at ~540 cm^{-1}, mainly A_g vibrational mode) and stretching vibrations (at
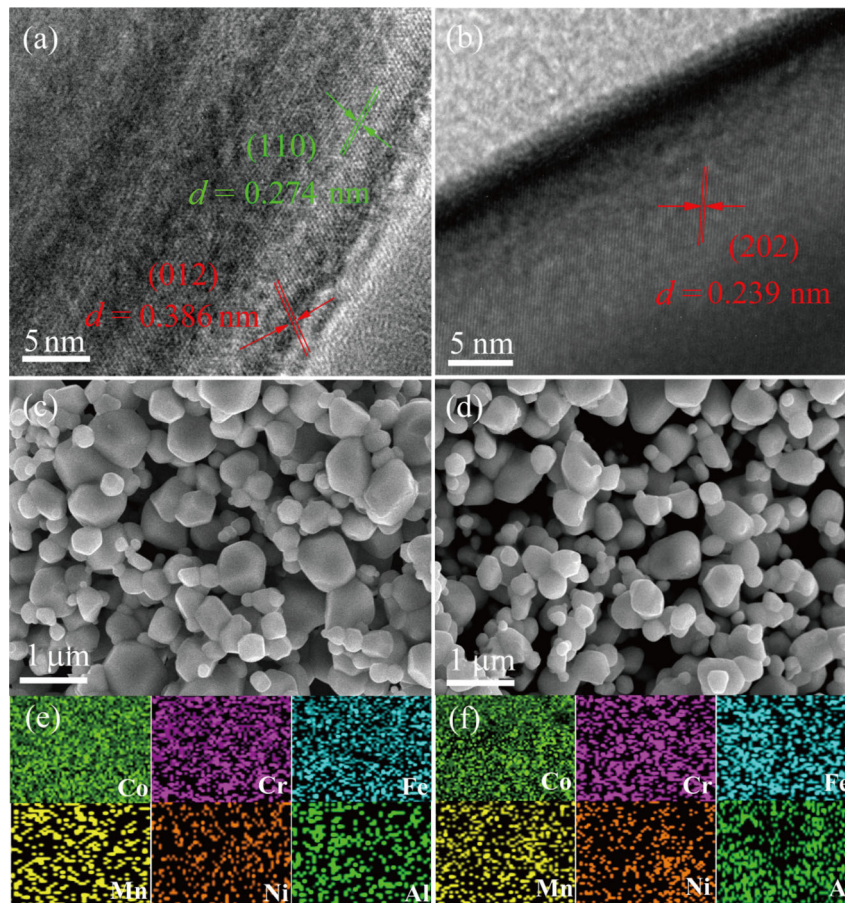
Fig. 4 HRTEM and SEM micrographs and related EDS elemental mappings for $La(CoCrFeMnNiAl_x)_{1/(5+x)}O_{3-\delta}$ samples: (a–c, e) $x = 0.5$; (d, f) $x = 0.7$.

~650 cm^{-1}, mainly B$_g$ vibrational mode) of the O–B–O groups according to Gupta and Whang [40] or Orlovskaya *et al.* [39]. The phenomenon of the changes in the Raman spectra of HEPOs caused by the introduction of Al^{3+} is noteworthy. With the increase of Al^{3+} concentration, the positions of the bands at ~540 and ~650 cm^{-1} are shifted (Table 2), showing that the vibration modes of the B–O–B bond have been changed. The type of the B cations is related to the deflection of the oxygen atoms during vibration of the O–B–O bonds, and thus, the Al^{3+}-doping leads to the change of the position of the respective bands. It can also be observed that the intensity of the two main bands decreases with the increase of Al^{3+} concentration. Since Al^{3+} ion is smaller than other B cations, which affects the deflection amplitude of O–B–O bending and stretching vibration, and thus, the intensities of the band at ~660 and ~540 cm^{-1} significantly decreases. Furthermore, the decrease of intensity may originate from the formation of oxygen vacancies and the intensification of lattice distortion effect [41] due to the introduction of Al^{3+}.
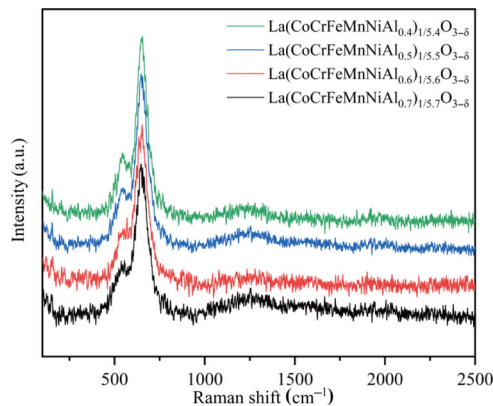

Fig. 5 Raman spectra recorded for the HEPO materials.

Table 2 Raman peaks of La(CoCrFeMnNiAl$_x$)$_{1/(5+x)}$O$_{3-\delta}$

| x	Area of the band $\times10^3$	Maximum of the band $\times10$	Position of the band (cm^{-1})
0.4	148.65	161.05	540.20
	407.41	475.04	653.16
0.5	142.74	146.69	537.93
	396.33	448.54	652.79
0.6	124.28	136.16	537.48
	385.99	403.12	650.03
0.7	119.67	120.81	534.47
	353.41	381.16	652.06

3. 2 Electrochemical properties of HEPO electrodes

In order to clarify the electrochemical properties of HEPOs, CV and GCD measurements were tested to obtain the specific capacitance. The CV was performed at different scan rates varying from 10, 20, 30, 40, 50, to 100 mV/s, with the potential range of 0–0.5 V. Figure 6 shows the CV curves of HEPOs with obvious oxidation and reduction peaks, indicating that they have typical pseudocapacitive characteristics. The capacitance of HEPOs can be attributed to the redox reaction of B-position cations, such as Co^{3+}–Co^{2+}, Cr^{3+}–Cr^{2+}, Fe^{3+}–Fe^{2+}, Mn^{3+}–Mn^{2+}, and Ni^{3+}–Ni^{2+}. The CV curves have no obvious shape distortion with an increase in the scan rate, suggesting that HEPOs have favorable reversibility and stability. Furthermore, these redox peaks are shifted to relatively higher and lower potentials with the increase of scan rate, owing to the polarization and ohmic resistance at the electrolyte–electrode interface during faradaic processes [6,42]. Even at a scan rate of 100 mV/s, the oxidation and reduction peaks of CV curve are still obvious, indicating that the materials have good rate performance [43]. As the scan rate increases, the absolute area of CV curves increases, and the specific capacitance decreases. At a lower scan rate, more electrolyte ions can move into the active material and participate in the electrochemical reaction occurred at the electrode surface, resulting in a higher specific capacitance [44]. The specific capacitances were evaluated according to the CV graphs at various scan rates using Eq. (1) [45]:

$$C = \frac{\int i\mathrm{d}V}{2mv\Delta V} \tag{1}$$

where C is the specific capacitance, m is the mass of the active material (g), v is the scan rate (mV/s), ΔV is the potential window (V), and $\int i\mathrm{d}V$ is the integral area of CV curve. The specific capacitances are summarized in Table 3.

GCD curves of HEPO electrodes at different current densities are shown in Fig. 7. The obvious plateau region appeared in GCD curves further reveals the pseudocapacitive behavior of the HEPOs. Table 4 shows the specific capacitances calculated by Eq. (2) at different current densities [46]:
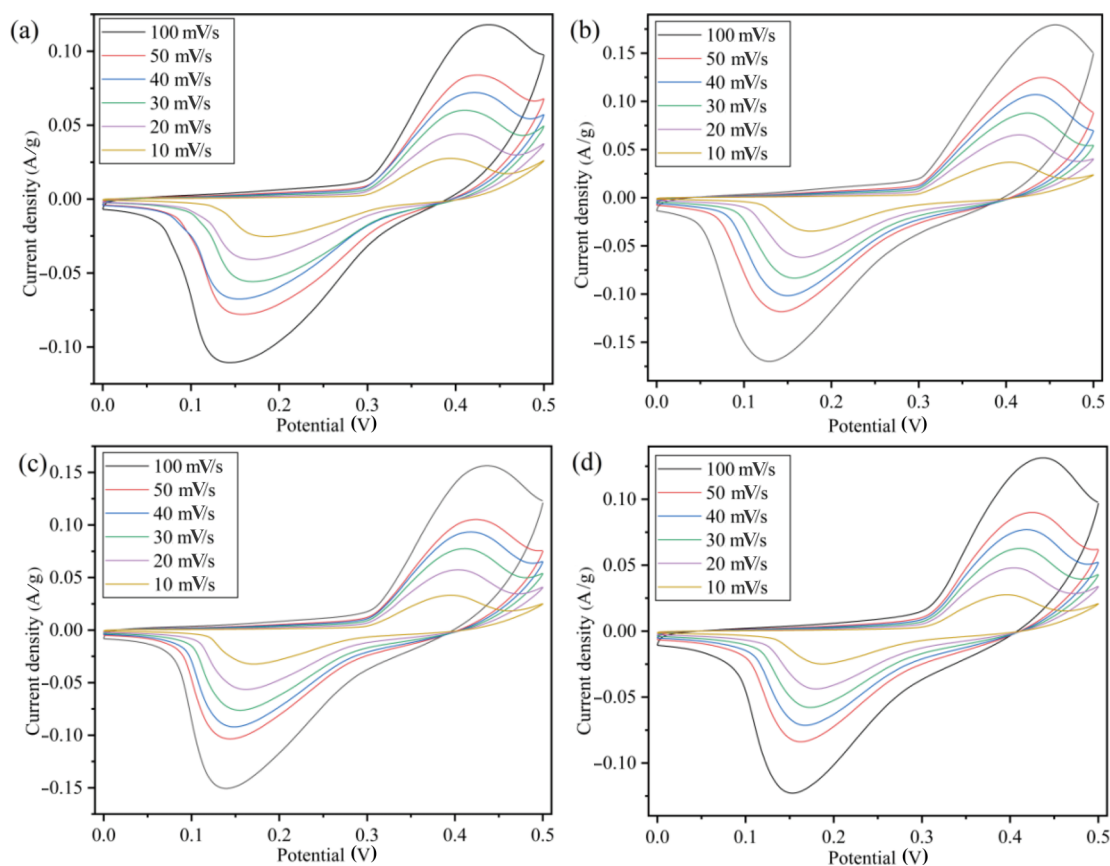
Fig. 6 CV curves of La(CoCrFeMnNiAl$_x$)$_{1/(5+x)}$O$_{3-\delta}$: (a) $x = 0.4$, (b) $x = 0.5$, (c) $x = 0.6$, and (d) $x = 0.7$.

Table 3 Specific capacitances of La(CoCrFeMnNiAl$_x$)$_{1/(5+x)}$O$_{3-\delta}$ at different scan rates

(Unit: F/g)

x	Scan rate (mV/s)					
	10	20	30	40	50	100
0.4	177.20	156.48	130.29	124.16	116.02	83.96
0.5	214.56	197.34	182.10	171.66	161.22	125.89
0.6	200.75	180.20	166.32	153.81	141.04	106.17
0.7	162.80	145.72	130.52	122.74	114.55	88.10

$$C = \frac{2i_{\mathrm{m}}\int V\mathrm{d}t}{V_1^2 - V_0^2} \qquad (2)$$

where i_{m} is the current density (A/g), V_1 and V_0 are the maximum and minimum values of the potential window (V), respectively, and $\int V\mathrm{d}t$ is the integral area of GCD curve. At higher current density, the time provided for the diffusion of ions is relatively small, which is why the C value is reduced with the increase of current density.

Stable cycling performance is essential for the application of supercapacitors. According to the GCD curve at a current density of 1 A/g, the cycle stability was tested by specific capacitances and the number of cycles. The charge–discharge cycles of HEPOs with the numbers up to 2000 are depicted in Fig. 8. After 2000 cycles, the specific capacitances of HEPOs with x ranging from 0.4, 0.5, 0.6, to 0.7 remain 85.01%, 88.61%, 86.37%, and 91.25%, respectively, showing the excellent cycle stability and charge–discharge reversibility of these electrode materials. The La(CoCrFeMnNi)$_{0.2}$O$_{3-\delta}$ electrode was tested under the same conditions, and its specific capacitance changes from 161.47 to 128.85 F/g (retention rate = 79.80%). After the long-term cycling, the decrease of specific capacitance mainly due to the mechanical failure of the electrodes results in the abscission of the active materials from Ni foam [47]. Compared with the La(CoCrFeMnNi)$_{0.2}$O$_{3-\delta}$ electrode material [48], the performance of HEPOs has a great improvement, and the results can be attributed to the following factors. Firstly, the inactive Al^{3+} can prevent the agglomeration of active ions and make these ions effectively participate in redox reaction. Secondly, Al^{3+}
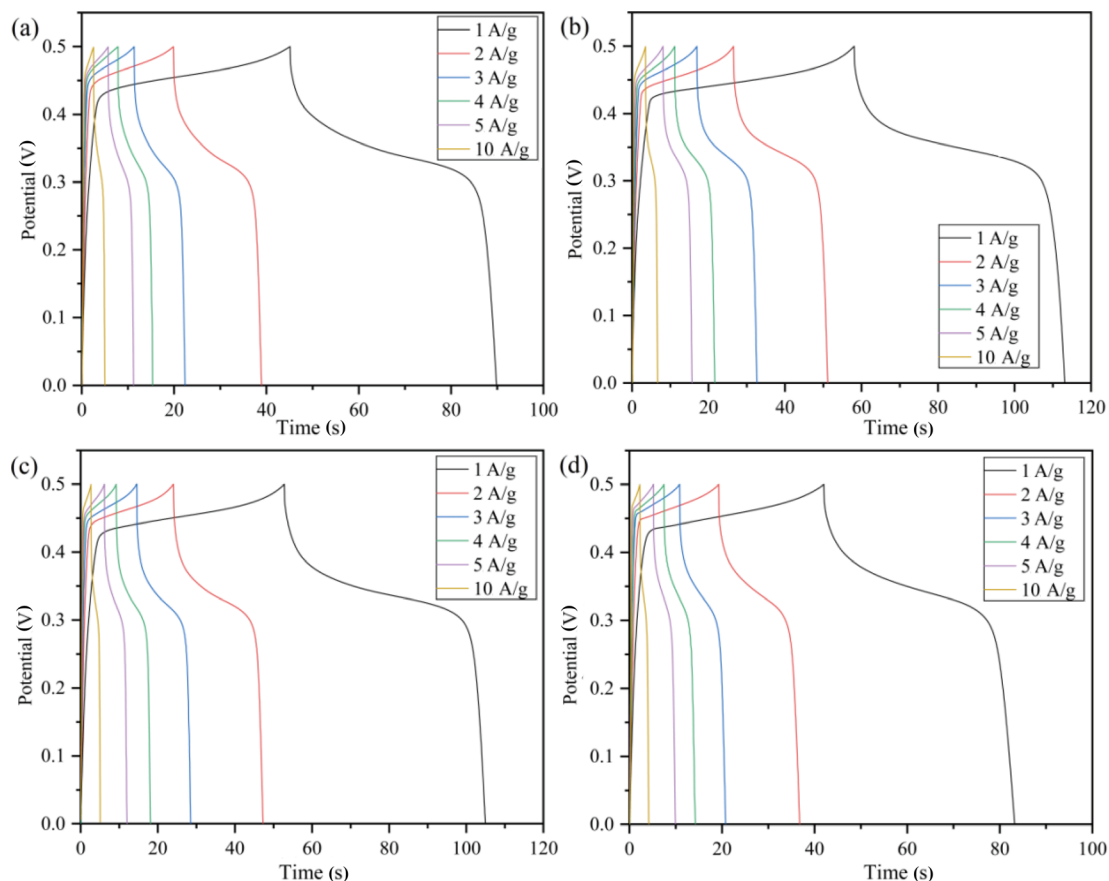
Fig. 7 GCD curves of La(CoCrFeMnNiAl$_x$)$_{1/(5+x)}$O$_{3-\delta}$: (a) x = 0.4, (b) x = 0.5, (c) x = 0.6, and (d) x = 0.7.

radius is quite different from the radit of other B-site ions that can produce lattice distortion and defects to retard crack propagation during charge–discharge process [19]. Transition metal oxides begin to agglomerate upon charge–discharge cycling, and then the secondary particles agglomerate, leading to the formation of the penetrating cracks. The capacity decreases mainly due to the loss of contact of the electrode with the current collector caused by crack propagation. Moreover, the lattice contraction caused by Al^{3+}-doping can enhance the binding force among the main atoms and produce a more stable crystal structure during charge–discharge cycle. Finally, the Al^{3+}-doping increases the configurational entropy and further improves the crystal structural stability, which results in an excellent cycling performance. With the increase of the Al^{3+} amount, more defects and the lattice distortion can be produced to prevent crack propagation, thereby providing higher cycle stability and specific capacitance. However, when the lattice distortion degree is too big, the ion migration is blocked, resulting in the reduction of the specific capacitances. As can be seen from Table 4,

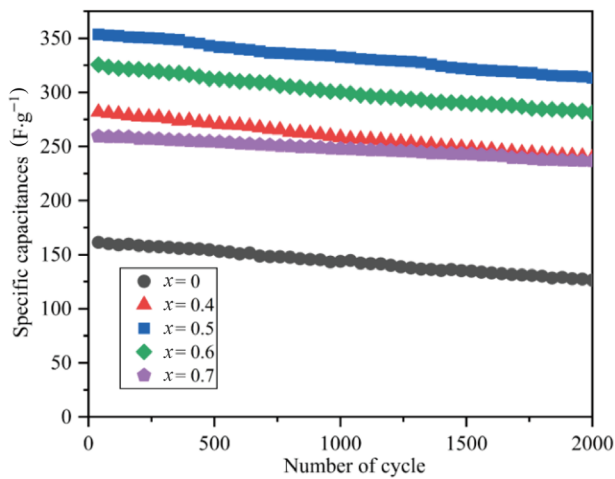**Table 4** Specific capacitances of La(CoCrFeMnNiAl$_x$)$_{1/(5+x)}$O$_{3-\delta}$ at different current densities

(Unit: F/g)

x	i_m (A/g)					
	1	2	3	4	5	10
0.4	281.84	244.80	209.44	180.24	173.34	145.76
0.5	353.65	319.56	304.94	266.87	241.63	208.75
0.6	325.60	294.69	264.72	233.31	182.88	149.89
0.7	259.30	230.66	193.82	174.36	152.70	121.37

the specific capacitances of the HEPO electrodes increase first, and then reduce with x ranging from 0.4, 0.5, 0.6, to 0.7, while the stabilities of HEPOs are increasing.

X-ray photoelectron spectroscopy (XPS) was carried out to investigate the chemical state variation in La(CoCrFeMnNiAl$_{0.5}$)$_{1/5.5}$O$_{3-\delta}$ during the redox reaction process. The typical XPS survey (Fig. 9(a)) reveals the coexistence of aluminum, cobalt, chromium, ferrum, manganese, nickel, and oxygen. As shown in Fig. 9(b), the Al 2p spectrum shows a remarkable signal

Fig. 8 Specific capacitance of La(CoCrFeMnNiAl$_x$)$_{1/(5+x)}$O$_{3-\delta}$ retention analyzed for 2000 GCD cycles at a current density of 1 A/g.
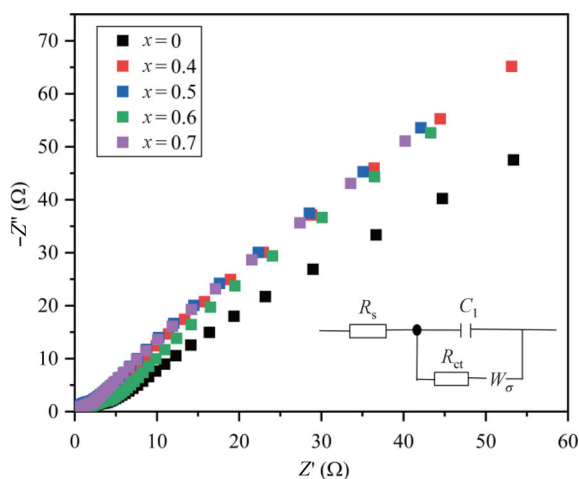
located at 72.7 eV, suggesting that Al is in a stable valence state of +3 [49]. The binding energies of Co 2p (Fig. 9(c)) are 779.4, 781.9, 794.5, and 795.4 eV, indicating the Co^{3+} and Co^{2+} cations in HEPOs. At the same time, two shake-up satellite peaks (defined as S$_1$ and S$_2$) confirm the coexistence of Co^{2+} and Co^{3+} species [50]. The Cr 2p spectrum (Fig. 9(d)) exhibits the Cr 2p$_{3/2}$ (576.4 eV) and Cr 2p$_{1/2}$ peak (586.1 eV), demonstrating the presence of Cr^{3+} species [51]. Similarly, the characteristic peaks of Fe 2p$_{3/2}$ and Fe 2p$_{1/2}$ at the Fe 2p spectrum (Fig. 9(e)) affirm the Fe valance states as Fe^{2+} and Fe^{3+}, accompanied with the shake-up satellite peak. The peaks at 709.8 and 722.6 eV are indexed to Fe^{2+}, and the peaks at 712.4 and 725.0 eV are related to Fe^{3+} [51]. Concerning the spectrum of Mn 2p in Fig. 9(f), it can be readily
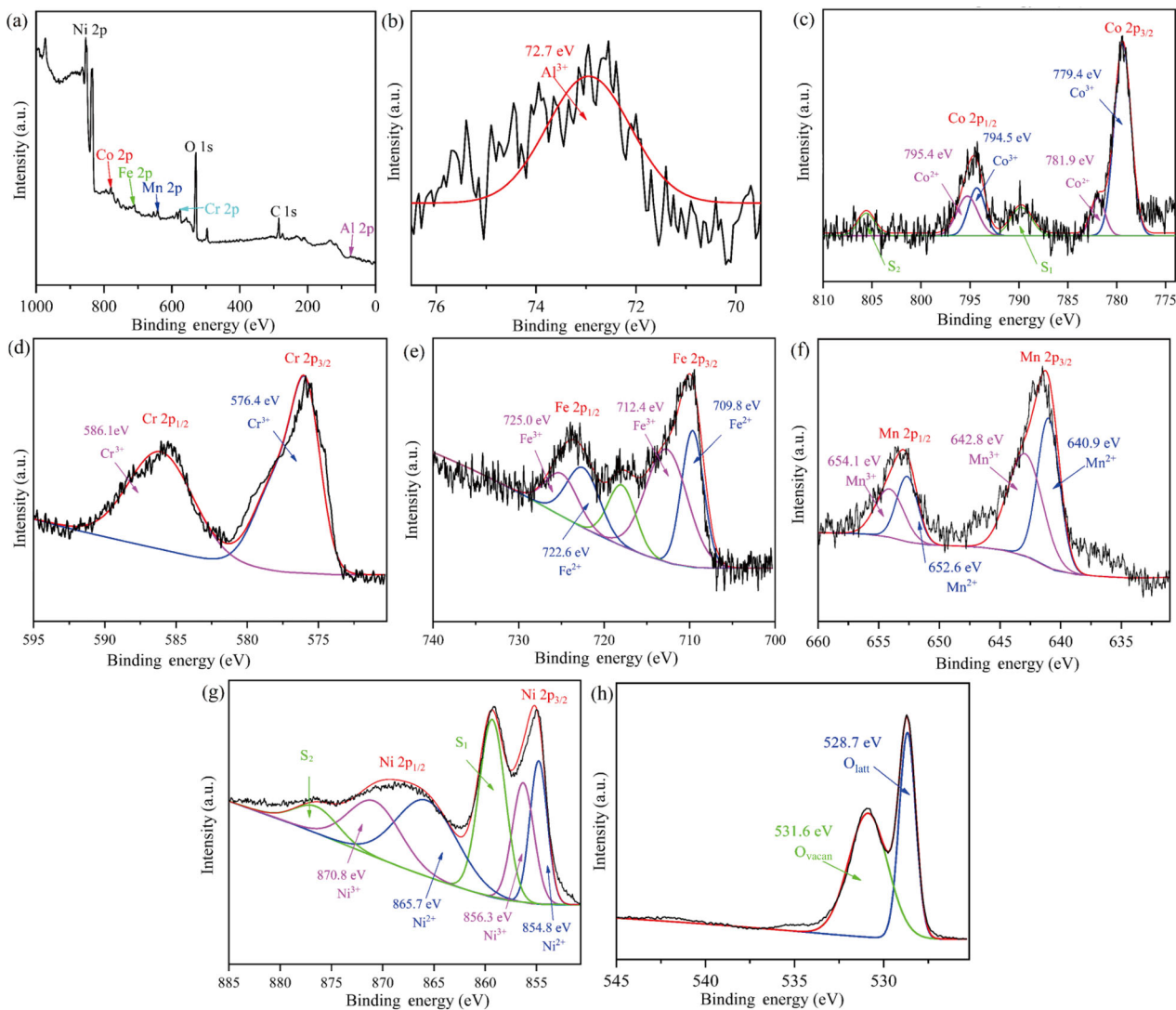
Fig. 9 XPS spectra of La(CoCrFeMnNiAl$_{0.5}$)$_{1/5.5}$O$_{3-\delta}$.

observed that the main peaks at 640.9 eV (Mn $2p_{3/2}$) and 652.6 eV (Mn $2p_{1/2}$) are indexed to Mn^{2+} species, and the peaks at 642.8 eV (Mn $2p_{3/2}$) and 654.1 eV (Mn $2p_{1/2}$) are related to Mn^{3+} species [52]. The spectrum of Ni 2p shown in Fig. 9(g) also confirms the coexistence of Ni^{2+} and Ni^{3+} species [50]. The presence of oxygen vacancy is revealed in the high-resolution O 1s spectra as shown in Fig. 9(h). Two intense peaks located at 528.7 and 531.6 eV correspond to the lattice oxygen (O_{latt}, M–O in the sample) and oxygen vacancy (O_{vacan}), respectively [51]. According to the ratio of the peak area, the O_{vacan}/O_{total} is calculated to be 49.8%. Therefore, it is believed that the high concentration of the oxygen vacancies increases the ionic conductivity and provides more active site, effectively enhancing the electrochemical performance.

The EIS analysis was implemented in the frequency region ranging from 10 mHz to 100 kHz. Figure 10 shows the Nyquist plot after fitting, with an oblique line at the low frequency and an absence of semicircle at the high frequency. As depicted in Fig. 10, the equivalent circuit includes electrolyte solution resistance (R_s), interfacial faradaic charge transfer resistance (R_{ct}), Warburg resistance (W_σ), and capacitance (C). The absence of semicircle is caused by the low charge transfer resistance at the working electrode–electrolyte interface and the rapid charge diffusion between the electrolyte and HEPOs [53]. It can be found that in the low frequency region, the Nyquist plot of Al^{3+}-doped HEPO is closer to the y axis than that of $La(CoCrFeMnNi)_{0.2}O_{3-\delta}$ electrode, which indicates

that Al^{3+}-doped HEPO electrodes have lower diffusion impedance and faster ion diffusion.

4　Conclusions

In summary, $La(CoCrFeMnNiAl_x)_{1/(5+x)}O_{3-\delta}$ (x = 0.4, 0.5, 0.6, and 0.7) HEPOs have been proposed by coprecipitation method combined with calcination process. Both the XRD and TEM results demonstrate that the synthesized oxide powders are assignable to R-3c perovskite structure. The electrochemical properties of HEPOs as supercapacitor electrodes were researched. The specific capacitances of HEPOs (x = 0.4, 0.5, 0.6, and 0.7) are 281.84, 353.65, 325.60, and 259.30 F/g at the current density of 1 A/g, respectively. The HEPO electrodes display outstanding capacity retention (remain 85.01%, 88.61%, 86.37%, and 91.25% after 2000 cycles). Among all the compositions, $La(CoCrFeMnNiAl_{0.5})_{1/5.5}O_{3-\delta}$ has the highest specific capacity and excellent cyclic stability, so the best doping for Al is x = 0.5. This research propagates the potential applications of HEOxs as supercapacitor electrodes, and provides a promising attempt for the design of HEOPs by introducing inactive ions to optimize electrochemical properties.

Fig. 10 Electrochemical impedance spectra of $La(CoCrFeMnNiAl_x)_{1/(5+x)}O_{3-\delta}$. Z' represents the real part of the impedance and $-Z''$ represents the negative number of the imaginary part of the impedance.

References

[1] Chaudhary S, Raja M, Sinha OP. A review on the different types of electrode materials for aqueous supercapacitor applications. *Adv Nat Sci*: *Nanosci Nanotechnol* 2021, **12**: 015011.

[2] Akkerman QA, Gandini M, di Stasio F, *et al*. Strongly emissive perovskite nanocrystal inks for high-voltage solar cells. *Nat Energy* 2017, **2**: 16194.

[3] Jia XT, Ge Y, Shao L, *et al*. Tunable conducting polymers: Toward sustainable and versatile batteries. *ACS Sustain Chem Eng* 2019, **7**: 14321–14340.

[4] Zhang DD, Li J, Su Z, *et al*. Electrospun polyporous VN nanofibers for symmetric all-solid-state supercapacitors. *J*

Adv Ceram 2018, **7**: 246–255.

[5] Hu QL, Yue B, Shao HY, *et al*. Facile syntheses of perovskite type LaMO₃ (M = Fe, Co, Ni) nanofibers for high performance supercapacitor electrodes and lithium-ion battery anodes. *J Alloys Compd* 2021, **852**: 157002.

[6] Kitchamsetti N, Choudhary RJ, Phase DM, *et al*. Structural correlation of a nanoparticle-embedded mesoporous CoTiO₃ perovskite for an efficient electrochemical supercapacitor. *RSC Adv* 2020, **10**: 23446–23456.

[7] Pu J, Wang X, Xu R, *et al*. Highly flexible, foldable, and rollable microsupercapacitors on an ultrathin polyimide substrate with high power density. *Microsyst Nanoeng* 2018, **4**: 16.

[8] Gao M, Wang WK, Rong Q, *et al*. Porous ZnO-coated Co₃O₄ nanorod as a high-energy-density supercapacitor material. *ACS Appl Mater Interfaces* 2018, **10**: 23163–23173.

[9] Ramirez-Castro C, Schütter C, Passerini S, *et al*. Microporous carbonaceous materials prepared from biowaste for supercapacitor application. *Electrochimica Acta* 2016, **206**: 452–457.

[10] Li Q, Xu YX, Zheng SS, *et al*. Recent progress in some amorphous materials for supercapacitors. *Small* 2018, **14**: e1800426.

[11] Simon P, Gogotsi Y. Perspectives for electrochemical capacitors and related devices. *Nat Mater* 2020, **19**: 1151–1163.

[12] Chen ZY, Chen YH, Zhao YZ, *et al*. B/N-enriched semi-conductive polymer film for micro-supercapacitors with AC line-filtering performance. *Langmuir* 2021, **37**: 2523–2531.

[13] Quispe-Garrido V, Cerron-Calle GA, Bazan-Aguilar A, *et al*. Advances in the design and application of transition metal oxide-based supercapacitors. *Open Chem* 2021, **19**: 709–725.

[14] Mefford JT, Hardin WG, Dai S, *et al*. Anion charge storage through oxygen intercalation in LaMnO₃ perovskite pseudocapacitor electrodes. *Nat Mater* 2014, **13**: 726–732.

[15] Guo GL, Ouyang K, Yu JP, *et al*. Facile synthesis of LaCoO₃ with a high oxygen vacancy concentration by the plasma etching technique for high-performance oxygen ion intercalation pseudocapacitors. *ACS Appl Energy Mater* 2020, **3**: 300–308.

[16] Rost CM, Sachet E, Borman T, *et al*. Entropy-stabilized oxides. *Nat Commun* 2015, **6**: 8485.

[17] Xiang HM, Xing Y, Dai FZ, *et al*. High-entropy ceramics: Present status, challenges, and a look forward. *J Adv Ceram* 2021, **10**: 385–441.

[18] Zheng YP, Zou MC, Zhang WY, *et al*. Electrical and thermal transport behaviours of high-entropy perovskite thermoelectric oxides. *J Adv Ceram* 2021, **10**: 377–384.

[19] Xiang HZ, Xie HX, Chen YX, *et al*. Porous spinel-type (Al₀.₂CoCrFeMnNi)₀.₅₈O₄₋δ high-entropy oxide as a novel high-performance anode material for lithium-ion batteries. *J Mater Sci* 2021, **56**: 8127–8142.

[20] Xu H, Zhang Z, Liu J, *et al*. Entropy-stabilized single-atom Pd catalysts via high-entropy fluorite oxide supports. *Nat Commun* 2020, **11**: 3908.

[21] Li F, Zhou L, Liu JX, *et al*. High-entropy pyrochlores with low thermal conductivity for thermal barrier coating materials. *J Adv Ceram* 2019, **8**: 576–582.

[22] Tseng KP, Yang Q, McCormack SJ, *et al*. High-entropy, phase-constrained, lanthanide sesquioxide. *J Am Ceram Soc* 2020, **103**: 569–576.

[23] Sun YN, Xiang HM, Dai FZ, *et al*. Preparation and properties of CMAS resistant bixbyite structured high-entropy oxides RE₂O₃ (RE = Sm, Eu, Er, Lu, Y, and Yb): Promising environmental barrier coating materials for Al₂O₃f/Al₂O₃ composites. *J Adv Ceram* 2021, **10**: 596–613.

[24] Chen H, Lin WW, Zhang ZH, *et al*. Mechanochemical synthesis of high entropy oxide materials under ambient conditions: Dispersion of catalysts via entropy maximization. *ACS Mater Lett* 2019, **1**: 83–88.

[25] Chen TY, Wang SY, Kuo CH, *et al*. In operando synchrotron X-ray studies of a novel spinel (Ni₀.₂Co₀.₂Mn₀.₂Fe₀.₂Ti₀.₂)₃O₄ high-entropy oxide for energy storage applications. *J Mater Chem A* 2020, **8**: 21756–21770.

[26] Li HY, Zhou Y, Liang ZH, *et al*. High-entropy oxides: Advanced research on electrical properties. *Coatings* 2021, **11**: 628.

[27] Banerjee R, Chatterjee S, Ranjan M, *et al*. High-entropy perovskites: An emergent class of oxide thermoelectrics with ultralow thermal conductivity. *ACS Sustain Chem Eng* 2020, **8**: 17022–17032.

[28] Sarkar A, Velasco L, Wang D, *et al*. High entropy oxides for reversible energy storage. *Nat Commun* 2018, **9**: 3400.

[29] Sarkar A, Wang QS, Schiele A, *et al*. High-entropy oxides: Fundamental aspects and electrochemical properties. *Adv Mater* 2019, **31**: e1806236.

[30] Bérardan D, Franger S, Meena AK, *et al*. Room temperature lithium superionic conductivity in high entropy oxides. *J Mater Chem A* 2016, **4**: 9536–9541.

[31] Qiu N, Chen H, Yang ZM, *et al*. A high entropy oxide (Mg₀.₂Co₀.₂Ni₀.₂Cu₀.₂Zn₀.₂O) with superior lithium storage performance. *J Alloys Compd* 2019, **777**: 767–774.

[32] Yan JH, Wang D, Zhang XY, *et al*. A high-entropy perovskite titanate lithium-ion battery anode. *J Mater Sci* 2020, **55**: 6942–6951.

[33] Dąbrowa J, Olszewska A, Falkenstein A, *et al*. An innovative approach to design SOFC air electrode materials: High entropy La₁₋ₓSrₓ(Co,Cr,Fe,Mn,Ni)O₃₋δ (x = 0, 0.1, 0.2, 0.3) perovskites synthesized by the sol–gel method. *J Mater Chem A* 2020, **8**: 24455–24468.

[34] Wang HB, Gao R, Li ZY, *et al*. Different effects of Al substitution for Mn or Fe on the structure and electrochemical properties of Na₀.₆₇Mn₀.₅Fe₀.₅O₂ as a sodium ion battery cathode material. *Inorg Chem* 2018, **57**: 5249–5257.

[35] Marrocchelli D, Perry NH, Bishop SR. Understanding chemical expansion in perovskite-structured oxides. *Phys*

Chem Chem Phys 2015, **17**: 10028–10039.

[36] Mo MY, Hui KS, Hong XT, *et al*. Improved cycling and rate performance of Sm-doped $LiNi_{0.5}Mn_{1.5}O_4$ cathode materials for 5 V lithium ion batteries. *Appl Surf Sci* 2014, **290**: 412–418.

[37] Zhou SY, Pu YP, Zhang QW, *et al*. Microstructure and dielectric properties of high entropy $Ba(Zr_{0.2}Ti_{0.2}Sn_{0.2}Hf_{0.2}Me_{0.2})O_3$ perovskite oxides. *Ceram Int* 2020, **46**: 7430–7437.

[38] Zhao L, Zhang J, Becker T, *et al*. Raman spectroscopy study of chromium deposition on $La_{0.6}Sr_{0.4}Co_{0.2}Fe_{0.8}O_{3-\delta}$ Cathode of solid oxide fuel cells. *J Electrochem Soc* 2014, **161**: F687–F693.

[39] Orlovskaya N, Coratolo A, Johnson C, *et al*. Structural characterization of lanthanum chromite perovskite coating deposited by magnetron sputtering on an iron-based chromium-containing alloy as a promising interconnect material for SOFCs. *J Am Ceram Soc* 2004, **87**: 1981–1987.

[40] Gupta RK, Whang CM. Structural study of a sol–gel derived novel solid oxide fuel cell perovskite: $(La_{1-x}Sr_x)(Cr_{0.85}Fe_{0.05}Co_{0.05}Ni_{0.05})O_{3-\delta}$. *J Phys*: *Condens Matter* 2007, **19**: 196209.

[41] Sarkar A, Loho C, Velasco L, *et al*. Multicomponent equiatomic rare earth oxides with a narrow band gap and associated praseodymium multivalency. *Dalton Trans* 2017, **46**: 12167–12176.

[42] Ji JY, Zhang LL, Ji HX, *et al*. Nanoporous $Ni(OH)_2$ thin film on 3D ultrathin-graphite foam for asymmetric supercapacitor. *ACS Nano* 2013, **7**: 6237–6243.

[43] Huo HH, Zhao YQ, Xu CL. 3D Ni_3S_2 nanosheet arrays supported on Ni foam for high-performance supercapacitor and non-enzymatic glucose detection. *J Mater Chem A* 2014, **2**: 15111–15117.

[44] Kumar M, Yun JH, Bhatt V, *et al*. Role of Ce^{3+} valence state and surface oxygen vacancies on enhanced electrochemical performance of single step solvothermally synthesized CeO_2 nanoparticles. *Electrochimica Acta* 2018, **284**: 709–720.

[45] Prasanna K, Santhoshkumar P, Jo YN, *et al*. Highly porous CeO_2 nanostructures prepared via combustion synthesis for supercapacitor applications. *Appl Surf Sci* 2018, **449**: 454–460.

[46] Zhang GX, Chen YM, He ZN, *et al*. Surfactant dependence of nanostructured $NiCo_2S_4$ films on Ni foam for superior electrochemical performance. *J Inorg Mater* 2018, **33**: 289–294. (in Chinese)

[47] Wang QF, Chen D, Zhang DH. Electrospun porous $CuCo_2O_4$ nanowire network electrode for asymmetric supercapacitors. *RSC Adv* 2015, **5**: 96448–96454.

[48] Guo M, Zhang FN, Miao Y, *et al*. Preparation and electrical properties of high entropy $La(Co_{0.2}Cr_{0.2}Fe_{0.2}Mn_{0.2}Ni_{0.2})O_3$ perovskite ceramics powder. *J Inorg Mater* 2021, **36**: 431.

[49] Lin JY, Hsu CC, Ho HP, *et al*. Sol–gel synthesis of aluminum doped lithium titanate anode material for lithium ion batteries. *Electrochimica Acta* 2013, **87**: 126–132.

[50] Sanchez JS, Pendashteh A, Palma J, *et al*. Porous NiCoMn ternary metal oxide/graphene nanocomposites for high performance hybrid energy storage devices. *Electrochimica Acta* 2018, **279**: 44–56.

[51] Biesinger MC, Payne BP, Grosvenor AP, *et al*. Resolving surface chemical states in XPS analysis of first row transition metals, oxides and hydroxides: Cr, Mn, Fe, Co and Ni. *Appl Surf Sci* 2011, **257**: 2717–2730.

[52] Liang BL, Ai YL, Wang YL, *et al*. Spinel-type $(FeCoCrMnZn)_3O_4$ high-entropy oxide: Facile preparation and supercapacitor performance. *Materials* 2020, **13**: 5798.

[53] Maiti S, Pramanik A, Mahanty S. Extraordinarily high pseudocapacitance of metal organic framework derived nanostructured cerium oxide. *Chem Commun* (*Camb*) 2014, **50**: 11717–11720.